UNIVERSITÀ DEGLI STUDI DI PADOVA

Dipartimento di Fisica e Astronomia "Galileo Galilei"

Corso di Laurea in Fisica

Tesi di Laurea

Design and application of diagnostic systems for an ICP plasma discharge

Progetto e realizzazione di diagnostiche per una scarica di plasma ICP

Relatore

Dr. Gianluigi Serianni

Correlatore

Dr.ssa Isabella Mario

Laureando

William Henri Vienne

Anno Accademico 2022/2023

Contents

1 Abstract

Neutral Beam Injectors for nuclear fusion require the production and acceleration of negative hydrogen ions. Negative ion sources are based on the inductive coupling of electromagnetic waves to a hydrogen plasma. To optimise the design of such sources, and particularly of the radiofrequency driver (the region where the plasma is generated), the MINION experiment is under realisation at Consorzio RFX (Padova) and the operations are starting. The first experimental phase will be devoted to plasma initiation and will require commissioning and testing of the various plants (pumping, gas injection, cooling, power supplies). The main outcome will be the identification and optimization of a reliable start-up process for the plasma. During the present thesis some diagnostic systems were developed and tested (capacitive probe) or calibrated (optical emission spectroscopy). Moreover, the first activities in view of the start of the plasma were performed, like the calibration of the pre-ionization filaments and the characterization of the gas injection and of the pumping system.

2 Sommario

Gli iniettori di fasci di particelle per la fusione nucleare richiedono la produzione ed accelerazione di ioni negativi di idrogeno. Le sorgenti di ioni negativi si basano sull'accoppiamento induttivo di onde elettromagnetiche ad un plasma di idrogeno. Per ottimizzare il progetto di tali sorgenti, e particolarmente del driver a radiofrequeza (la regione in cui si crea in plasma), si sta relaizzando l'esperimento MINION al Consorzio RFX (Padova) e si sta cominciando la sperimentazione. La prima fase speriemntale sarà dedicata all'innesco del plasma e richiederà la messa in servizio ed il test di vari impianti (pompaggio, immissione gas, raffreddamento, alimentazioni). Il principale risultato sarà l'identificazione ed ottimizzazione di un affidabile procedura di partenza del plasma. Durante questa tesi sono stati sviluppati e testati (sonde capacitive) o calibrati (spettrscopia ottica in emissione) vari strumenti di misura. Inoltre, sono state svolte le prime attività in vista dell'accensione del plasma, quali la calibrazione dei filamenti di pre-ionizzazione e la carattgerizzazione del sistema di immissione gas e di quello di pompaggio.

3 Introduction

The future fusion reactor ITER will adopt two neutral beam injectors (NBI) that provide up to 33 MW to the fusion plasma. The ITER NBI consists of a negative ion source, from which ions are extracted and accelerated to a maximum energy of 1 MeV in a multi-aperture multi-grid electrostatic accelerator system. The remaining ions in the beam are electrostatically removed.
A beam is composed by 1280 beamlets, each one with a divergence that must be between 3 and 7 mrad. To avoid poor beam trasmission and higher localized heat loads, each beamlet current has to differ by less than 10% from the average value.
SPIDER is a full size ITER NBI ion source operating in vacuum that started its operations in Padua in 2018. During early operations showed that a pressure below $p_{limit} = 40$ mPa was needed to avoid discharge on the back of the RF drivers.
The system suffers from limited power coupling efficiency as it is estimated that only 40 % of the generator output is coupled with the plasma, while the rest is coupled with the passive structures.
As it was planned to achieve a generated power of 100 kW/driver for each one of the eight drivers, the achieved power was limited to 70 kW/driver wiht only one operating driver and 50 kW/driver when more than two driver were operating.
In addition, the 12 mrad beamlet divergence exceeded the target 7 mrad divergenge for ITER NBI, probably due to a large negative ion temperature.
Also, if the proportionality between the extract current density and the RF power is assumed, a driver power of 105 kW would be necessary to extract a current of 355 A/m^2, just enough for ITER requirements.
A test stand was developed, dubbed MINION (Magntized ICP for Negative Ion Operation in NBI), was developed in order to optimize different key factors in extraction of a neutral beam, such as: a better setup for RF driver setup,optimization of the expansion region, improvement of plasma confinement, understanding of RF plasma physics in negative ions sources, test of solid-state RF generators and of non-evaporable getter pumps.

MINION experiment consists of one RF driver, identical to those used in SPIDER, connected to a plasma box that will operate in vacuum. The vessel is divided in two halves, the top one is fixed over a metallic support structure, while the bottom one, which contains the driver and the plasma box, is attached to a movable system that allows vertical movement and horizontal movement on the ground.

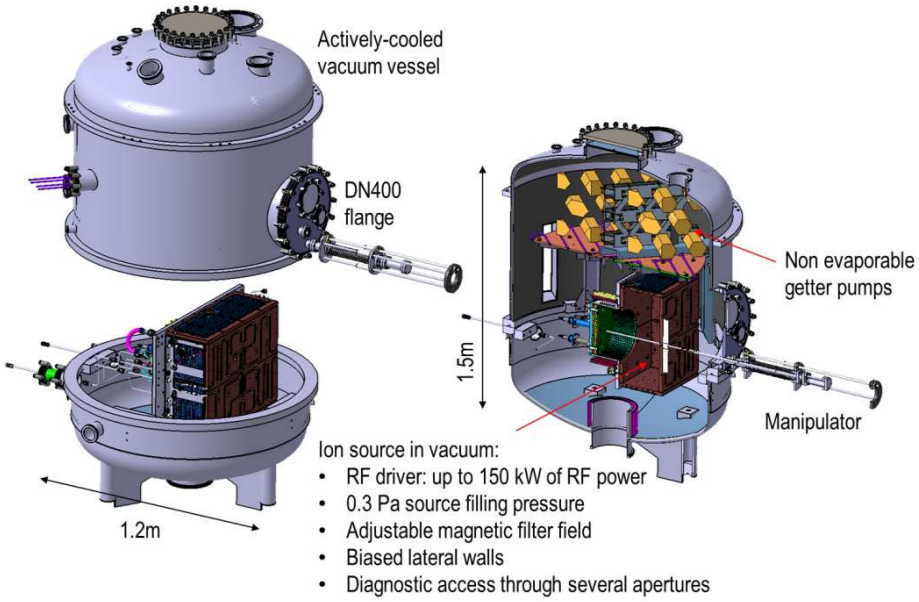

Figure 1: Schematic of MINION experiment. The vacuum vessel in grey and the plasma source in brow. On the left is shown how the two halves are divided, while in the right there is a vertical section of the vessel closed.

In figure 1 is shown a schematic of the MINION experiment. The plasma should face the DN400 flange, where a manipulator supports a Langmuir probe or other diagnostics systems that can reach the bottom of the RF driver.

The present thesis describes the activities in preparation of the operations with MINION.

4 Development of capacitive probes for MINION

Capacitive probes are electrodes inserted into plasma that, based on the capacitive coupling between the Debye sheath and the probe, can measure the amplitude of the RF component and of its harmonics in the plasma.
Their design is quite simple, the materials are easy to retrieve and to substitute and do not need auxiliary circuitry, like RF compensation for the Langmuir probes.

The idea is that the probe tip, inserted into the plasma, is able to follow the po-

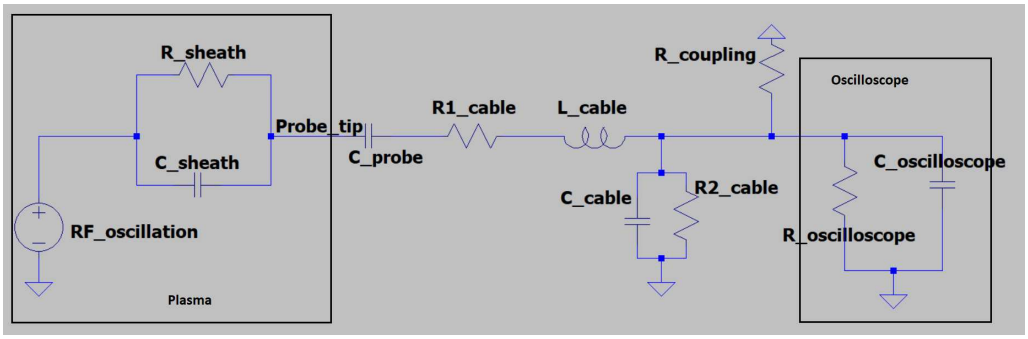

Figure 2: Circuit model for the capacitive probe

tential of the plasma if certain conditions are met. The most important one is that the ratio between the capacitance of the probe and the capacitance of the sheath is really small, like around 5%.
There are different designs possible for the probe, so as to maintain a defined ratio between the sheath and the probe capacitance. The one that has been chosen is a rectangular tip made in copper, as it is quite simple to control the interaction area and the dimension of the sheath generated. Inside the tip of the probe, with walls in kapton, a capacitor needs to be installed. The capacitance is estimated the as a plain capacitor $C = \epsilon_r \epsilon_0 \frac{S}{d}$, where ϵ_r is the relative permittivity, ϵ_0 is the vacuum permittivity, S is the surface of the capacitor and d is the distance between the two extremal kapton faces. A copper filament is inside the capacitor and is attached to a 20 cm of Kap-4 cable.
The latter is then welded to a BNC connector, where the cables can be mounted to connect the probe to the measurement system.
In figure 2 a circuit model of how the plasma interacts with the probe connected to the measurement system is shown. It is important to say that C_{sheat} and R_{sheath} depend from the shape and surface of the electrode inserted, and they are not constant over time if an RF oscillation is present.

4.1 Simulations

Upon modelling the circuit in figure 2 by LT-Spice, some calculations were made in order to give an estimate of the sheath capacitance C_{sheath}, so that the dimension of the capacitor that would be installed inside the probe tip are estimated.
Based on the data from the CRISP experiment, the one where the first test of the probe was carried out, those plasma parameters were assumed:

Parameter	Value
kT_e	$10\ eV$
Effective mass	$4\ amu$
Electron density	$2 * 10^{16}\ m^{-3}$

Table 1: Assumed parameters for a pseudo capacitive discharge in CRISP

Then the length of the Debye sheath was estimated, in the approximation of $quasi - static$ ions, as it follows:

$$\lambda_D = \sqrt{\frac{\epsilon_0 k T_e}{n e^2}} \tag{4.1}$$

The first approximation of the sheath capacitance can be expressed as:

$$C_0 = \frac{\epsilon_0 A_p}{2^{\frac{7}{4}} \lambda_D} \left(\frac{e(V_{DC} - V_P)}{kT_e} \right)^{-\frac{3}{4}} \tag{4.2}$$

where A_p is area of the probe, V_{DC} is the potential of the probe if there is no RF potential is present, and V_p is the plasma potential. However, since a magnetic field is present, some correction should be applied for better results. In particular, a logarithmic corrective term that takes into consideration the effective collection area and the effective mass of the helium ion of the gas:

$$C_0 = \frac{\epsilon_0 A_p}{2^{\frac{7}{4}} \lambda_D} ln \left(\left(\frac{A_{eff}}{A_{geo}} \right) \left(\sqrt{\frac{2}{\pi} M_{eff} \frac{M}{m_e}} \right) \right)^{-\frac{3}{4}} \tag{4.3}$$

Where the term under the square root comes from the expression of the floating potential:

$$V_f = V_s - \frac{kT_e}{2e} ln \left(\frac{2M}{\pi m} \right) \tag{4.4}$$

Another approximation is given by the fact that the geometric area of a tip of the order of some cm^2 is not appreciably modified if some Debye lengths of collection are added to the rectangle sides.
The simulations showed that, with a fixed sheath capacitance of some pF, the response function has a really high slope, as it can be seen in figure 3.

This means that, even if small errors are committed while choosing the simulation parameters, the errors on the attenuation will be quite big, and a calibration will be needed in order to choose the right attenuation value to convert the potential registered by the oscilloscope into the plasma potential.

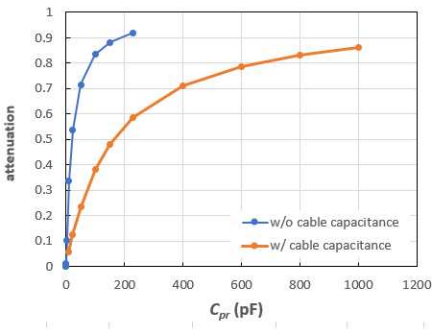

Figure 3: Response function of the probe with and without cables stray impedances.

Then the values of the probe surface were changed, trying to find a good balance between the surface dimension, the sheath capacitance and the probe capacitance that has to be really small, of the order of $10^{-1}pF$ so that the coupling is effective.
After some tests, it was opted for a probe surface of 8 cm^2 (only one face contributes to the collection of signals since the other face is attached to the vessel), with an estimated sheath capacitance of 4.30 pF with an internal capacitor of the order of the 0.1 pF and an expected attenuation of one part over one thousand.

4.2 Realization of the probe

After defining its characteristics, the probe was realized using two rectangular pieces of copper, with a surface of $(2x4)$ cm, a capacitor with kapton layers as plates of a surface or $2.25 * 2.25$ mm and a thickness of 0.4 mm placed as shown in figure 4. Since the kapton layers and the silicon glue that keeps them together have a relative dielectric coefficient of $\epsilon \approx 3$, the expected value of the capacitance of the probe is 0.336 pF.

Figure 4: The detail of the inside of the probe. The red highlighted area is the katpon layers.

Figure 5: The probe tip sealed with insulated connector to the Kap4 cable.

The final result of the probe is shown in figure 5. It can be seen that the copper surfaces have been welded together to be sure that the glue inside will not isolate

the two pieces, and the connection between the Kap4 cable and the probe has been insulated as much as possible, trying to avoid any stray impedances.

4.3 Calibration of the capacitive probe

The probe was calibrated by generating sinusoidal signals with a Tektronix AFG3012B function generator at different frequencies and by measuring the output signals with a Yokogawa DL9040 digital oscilloscope.

The output of the function generator was attached to the copper electrode, so as to simulate the signal that could be collected in plasma; one probe of the oscilloscope was installed in the same position. Then, a coaxial cable connected the capacitive probe, via a BNC connector, to the second channel of the oscilloscope, so that it was possible in real time to measure the input signals, the output from the capacitive probe, thus estimating the order of the attenuation.

Figure 7 show all the values of attenuation obtained at different frequencies.

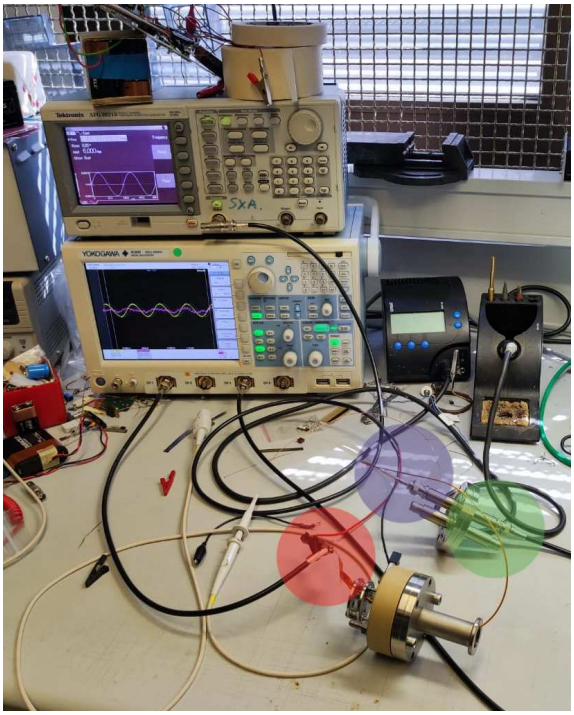

Figure 6: The calibration setup. In red is highlighted the function generator connector attached to the probe tip and the probe connected to the first channel of the oscilloscope, in blue the connector between the probe and the external cable, and in green the cable connected from the probe to channel three of the oscilloscope.

Even if the attenuation is of the order of few parts per thousand, an exit signal still well distinguishable by an oscilloscope, as expected by the simulations.

After the data has been collected, a linear fit was executed, as shown in figure 7 in order to be able to convert the collected signal in estimates of plasma potential with *RF* oscillations during the testing.

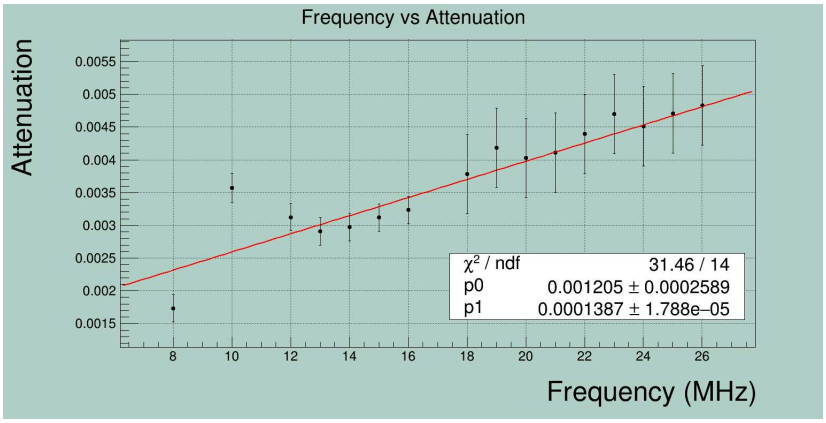

Figure 7: Linear fit of Frequency vs Attenuation

4.4 Tests in the CRISP experiment

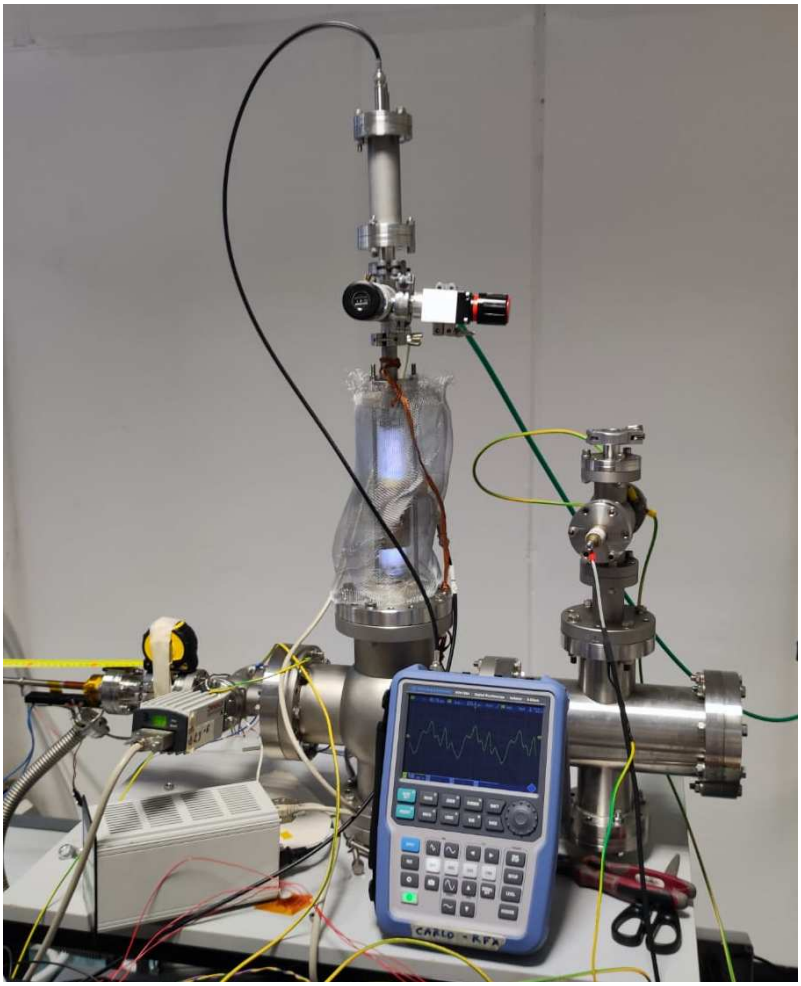

Figure 8: The plasma inside the CRISP experiment turned on with the probe inside the plasma region. On the oscilloscope it is visible the third harmonic.

After verifying that the probe responds essentially has expected, it was placed inside the CRISP experiment, where a pseudo-capacitive discharge in He can be created.

The first thing done was to change the frequency of the oscillation in the plasma, to turn it on and to have the best SWR value possible.
Then, as soon as the plasma exhibits the bright blue color of helium plasma, the probe was connected to the oscilloscope and the data in table 2 was recorded.
Since the particle density is one of the key factors for the dimension of the Debye sheath, the change of pressure and, by consequence, the number of particle inside the system has repercussion on the signal detected by the probe, as the peak to peak potential lower till almost a constant value.

f (MHz)	$p_{injection}$ (mbar)	p_{vessel} (mbar)	$p_{discharge}$ (Pa)	V_{pp} (mV)	$V_{pp}^{plasma}(V)$
29.6	0.001116	0.000744	0.093	290	55 ± 3
29.6	0.0124	0.000938	0.6669	250	47 ± 2
29.6	0.025	0.00129	1.3145	100	19 ± 1
29.6	0.035	0.0016	1.83	55	10.4 ± 0.5
29.6	0.049	0.00207	2.5535	53	10.0 ± 0.5
29.6	0.065	0.00278	3.389	48	9.1 ± 0.5

Table 2: Data acquired with the probe at fixed frequency and different pressures

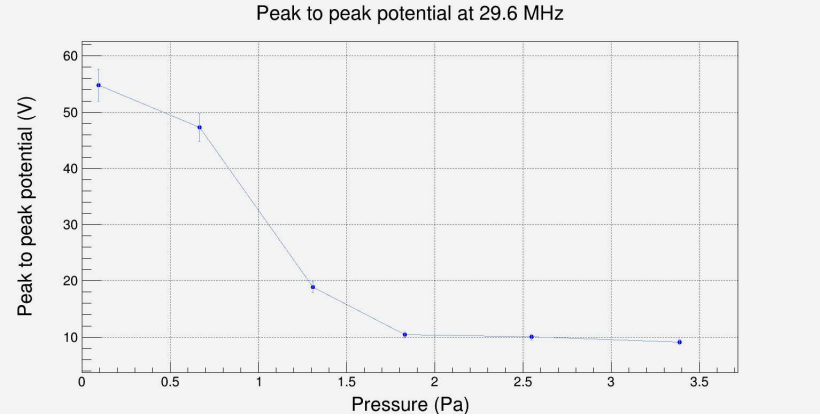

Figure 9: Peak to Peak plasma potential as a function of pressure

Then, the pressure was fixed and frequency of the oscillation was changed with 0.2 MHz steps and the results are shown in table 8 and the plot of the data in figure 10. The values of the SWR were recorded so as to understand how much energy was transferred from the coil to the plasma and if it could change the signal collected by the probe.
Overall, the attenuation obtained by the probe during the tests is similar to expectancy, even if a bigger attenuation value, which, if the approximate model is applied, the inside capacitance is of the order of 0.6 pF, and the ratio between V_{Probe}/V_{Plasma} is 97% circa.
The results show that the overall behaviour is similar to what was expected. Hence,

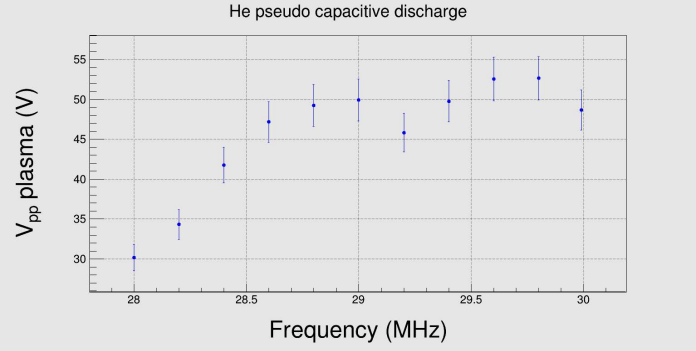

Figure 10: Plot of frequency vs peak to peak plasma potential

it is possible to build a capacitive probe that will follow the *RF* oscillations of plasma with a signal not too affected by the stray impedance of the cables, even if they possess such a small capacitance.

5 MINION spectroscopy

5.1 Basics of plasma spectroscopy

Emission plasma spectroscopy is one fundamental tool for the study of plasma parameters as it can give real-time observations while not being invasive, as plasma is not affected since the lenses and the acquisition system are not in contact with the plasma. Some drawbacks are the cost of such systems and the not straightforward interpretation of the emission spectra.
Radiation emission is generated by atomic and molecular electronic transitions. When atoms or molecules are excited and electrons transition from a ground state (0) to an energy level (p), and then decay to a level (q), the resulting emitted wavelength can be calculated as follows:

$$\lambda = \frac{hc}{E_p - E_q} \tag{5.1}$$

where h denotes the Planck constant, c the speed of light, $(E_p - E_q)$ energy difference of the electron from state (p) to state (q).
The intensity of the emitted radiation can be expressed as:

$$\epsilon_{pq} = n_p A_{pq} \frac{hc}{4\pi\lambda} \qquad\qquad \epsilon_{pq} = n_p A_{pq} \frac{h\nu}{4\pi} \tag{5.2}$$

where ϵ_{pq} is called the line emission coefficient from state (p) to state (q), A_{pq} is the transition probability and ν denotes the frequency of the transition. If both the transition probability and the frequency are known, it is possible to get by direct measurement the line emission coefficient, to reverse the previous equation and to get the density of state p :

$$n_p = \frac{\epsilon_{pq} 4\pi}{A_{pq} h\nu} \tag{5.3}$$

Since the population density depends on plasma parameters such as the plasma temperature and the electron density, population models can be applied to extract information about the plasma.
The collisional radiative model for hydrogen describes the behaviour of hydrogen plasmas, as it takes into account collisional and radiative processes of excited molecules or atom populations in plasma.
In order to obtain the density of the different atoms and molecules in the plasma,

Process	Reaction
Excitation by e^-	$H(q) + e^- \longrightarrow H(p > q) + e^-$
De-excitation by e^- collision	$H(q) + e^- \longrightarrow H(p < q) + e^-$
Spontaneous emission	$H(q) \longrightarrow H(p < q) + h\nu$
Ionization	$H(q) + e^- \longrightarrow H^+ + 2e^-$
Recombination of H^+	$H^+ + 2e^- \longrightarrow H(p) + e^-$
	$H^+ + e^- \longrightarrow H(p) + h\nu$
Dissociation of H_2	$H_2 + e^- \longrightarrow H(p) + H(1) + e^-$
Dissociation of H_2^+	$H_2^+ + e^- \longrightarrow H(p) + H^+ + e^-$
Dissociative recombination of H_2^+	$H_2^+ + e^- \longrightarrow H(p) + H(1)$
Dissociative recombination of H_3^+	$H_3^+ + e^- \longrightarrow H(p) + H_2$
Mutual neutralization ($x = 1, ..., 3$)	$H_x^+ + H^- \longrightarrow H(p) + H(1)$

Table 3: Reactions included in the CR model for hydrogen plasma. Since in MINION the telescopes will be placed near the driver region, only direct excitation and dissociation are dominant.

rate equations are set up for the different populations n_p:

$$\frac{n_p}{dt} = \sum_{q>p} A_{qp} n_q - \sum_{q<p} A_{pq} n_p + n_e\Big(\sum_{q\neq p} X_{qp} n_q - \sum_{q\neq p} X_{pq} n_p + (\alpha + \beta n_e) n_+ - S_p n_p\Big) \tag{5.4}$$

where A_{pq} and A_{qp} are the transition probabilities of spontaneous emission from p to q and q to p respectively, α and β are the rate coefficients for recombination of an ion with density n_+ and S_p is the rate coefficient for the ionization of the state p and X_{pq} and X_{qp} are the rate coefficient for de-excitation and excitation by electron collision. As shown in table 3, different phenomena take place for hydrogen, but, given the proximity to the driver region of the telescopes in the MINION experiment, the model can be simplified by focusing on the most dominant effects: direct excitation and dissociative excitation, that in table 3 are reported in bold .

The easiest emissions lines to be detected and analyzed are those of the Balmer series, in particular the H_α, which corresponds to the transition from $n = 3$ to $n = 2$, with a wavelength of $656.3nm$, and the H_β, corresponding to the transition from $n = 4$ to $n = 2$, with a wavelength of $481.1nm$.

Particularly interesting are also the lines of the Fulcher series, which is a consequence of the dynamics of hydrogen molecules. However they are less intense, and to be distinguished highly diffractive gratings are needed.
Once obtained the line emission coefficients, it is possible to use collisional-radiative codes, like the *YACORA* package, to determine plasma parameters such as the density of the desired population and the electron temperature.

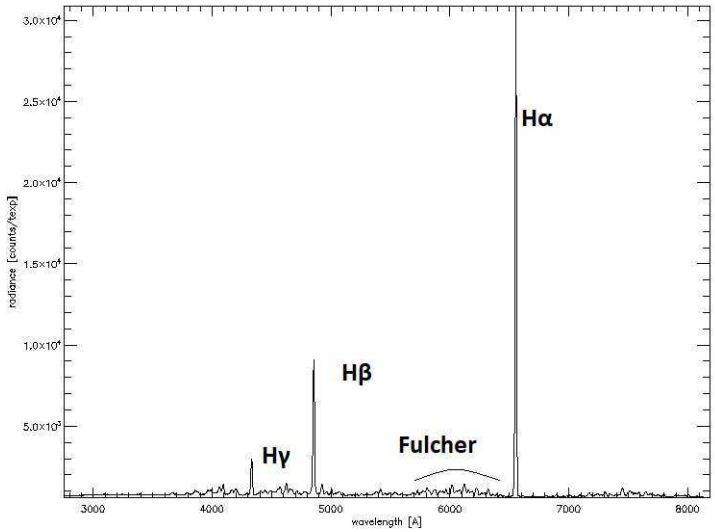

Figure 11: Low resolution spectrum of Hydrogen plasma with the first three lines of the Balmer series and the Fulcher hydrogen lines.

The *YACORA* package is able to evaluate the solutions of the rate equation described before for the different particle populations that are present in the reactions considered by the collisional-radiative model.

5.2 Experimental setup

5.2.1 Spectrograph

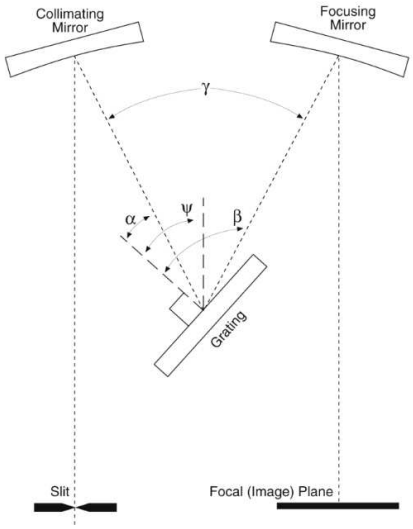

Figure 12: Czerny-Turner configuration of the spectrograph.

The acquisition system is composed by a 750 SpectraPro spectrograph and a PIXIS:2K camera with a 2048×512 imaging array and $(13.5x13.5)\mu\ m$ pixel dimension.

The spectrograph is provided with two entrance slits, one on the front and one on the side of the instrument, where optical fibers can be placed with the appropriate supports.

These slits can be adjusted using a small handle, allowing to control the amount of light entering in the system and avoiding background noise. During the measurement, an opening of $50\mu\ m$ was adopted, since the intensity of the

signal has a well defined Gaussian shape.

The spectrograph is arranged in the Czerny-Turner configuration as shown in figure 12: the light, which enters into the system from one of the slits, is directed to a concave mirror. This mirror, after collimating the light, directs it onto one of the three possible gratings with different groove density, for a different resolution of the spectra: $900\frac{g}{mm}$, $100\frac{g}{mm}$ and $50\frac{g}{mm}$. The light is then diffracted by the grating, and depending on the wavelength, is deflected by a certain angle. Then, the diffracted light encounters a focusing mirror, which focuses the light on the exit slit, where the camera records the spectral data.

5.2.2 Calibration of the telescopes

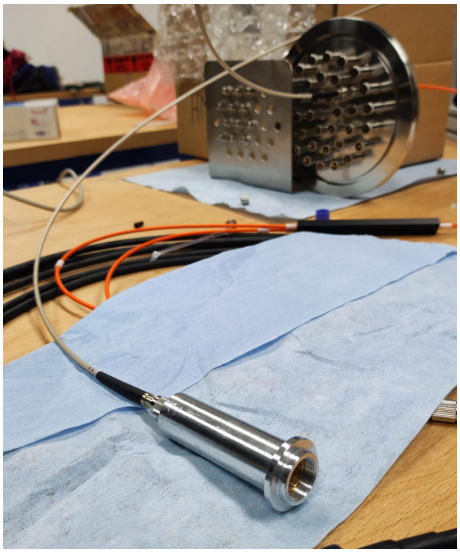

Figure 13: Telescope with 50 *cm* focal length and 10 *mm* diameter lens attached to the bezel with the optical fiber.

The telescopes adopted for the MINION diagnostic system are two cylinders that can slide one inside the other. One lens is inserted in the cylinder with the larger diameter, while the optical fiber is terminated in the other one. In this way it is possible to adjust the distance between the fiber and the lens, so as to modify the position where the image plane of the fiber is realized. It is important to understand which spatial region contributes to the collected light, and defines the spectra obtained, so as to avoid unwanted light sources, such as due to reflections, or simply not considered regions.
In order to study the shape of the light cone collected (Line of Sight or LOS), a white LED is attached to the optic fiber to illuminate the lens from the side where the instruments will be placed so an illuminated region is realized which will contain the plasma that will contribute to the collected light. As the telescopes are placed near or behind the driver region, where the plasma is characterized by direct and dissociative excitation, the light is much more intense than the light coming from the plasma in the expansion region and the previously described phenomena can be studied while ignoring recombination occurring in the expansion region.
The ideal shape of the LOS would be a cylinder with one base on the lens, and the other at around 40 *cm* from the lens, in order to collect the light from the plasma and avoid undesired sources. Of course this is impossible, so the best thing to do is

to try to get a diameter as constant as possible between 20 *cm* and 40 *cm* from the lens. Because of this, the lenses are focused beyond the plasma region.

The lenses that will be used are two with focal length of 50 *mm* and diameter of

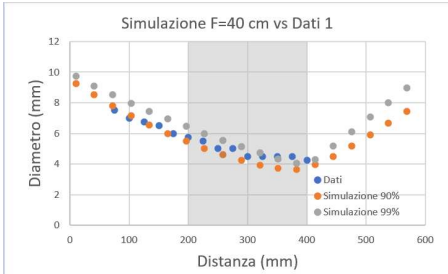

Figure 14: Measured diameter for 40 cm focal length lens.

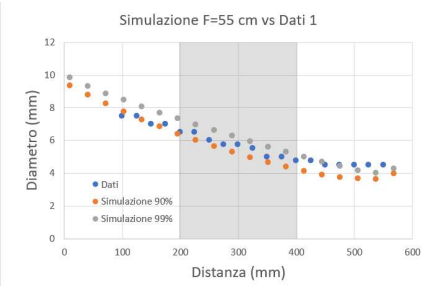

Figure 15: Measured diameter for 50 cm focal length lens.

10 *mm* and three with focal of 40 *mm* and diameter of 10 *mm*. Also one lens with focal length of 8 *mm* and diameter of 8 *mm* was studied, because of its reduced length, but the behaviour was problematic for reasons that will be explained.

Figure 16: The diameter of the 8 *mm* focal lens at 50 *cm* over graph paper. It is possible to see how big the divergence is.

All the telescopes were bench adjusted, by placing them over a rail, as the white LED backlights them, creating a light circle over a piece of graph paper placed over a movable support over the rail. The focus point was found in the prefixed spot by changing the distance between the fiber and the lenses. Then, every 2.5 *cm*, the diameter of the illuminated area over the graph paper was measured. The illuminated area has a clear-cut border, and is easy to measure, only in the proximity of the focal plane. However, even if the further away from the lens, the more subjective the criteria for the border becomes, it still has a relevance, as the human eye is able to detect quite well the area which contains the 90% of the light emitted by the LED.

From the data in figure 14 and 15, the shape of the LOS is quite cylindrical in the region we are interested in studying (the area with the gray background): from 20 *cm* beyond the lens till 40 *cm* from the lens, where the plasma is expected to be found.

For the 8 mm lens, the situation is different. Because of the short focal length, it is challenging to avoid a big divergence. This implies that the data analysis will be really hard, if not impossible, due to the inability to understand the light sources, such as unwanted reflections from the inside of the vessel.

For all the lenses, collected data were confronted with simulations. The latter return

the diameters of the light cones at different distances, for different light intensities, in particular at 10%, 50%, 90% and 99%. This comparison is based on knowledge of the lens focal length, the focal plane and the diameter of the fibers and of the lenses.
Since the human eye is only able to distinguish clearly around the 90%, the measured diameter on the plane was compared with the simulations data of 50%, 90% and 99%.
As expected, acquired data and simulations are compatible for 90% intensity, thus the LOS shape is known.

5.3 Wavelength calibration

The objectives of the wavelength calibration of the spectrograph is to assign a wavelength to the pixels of data acquired from the camera and to measure the instrumental resolution, which will determine the closest possible lines that will be distinguishable during data analysis.
In order to achieve this, the exact setup that will be used for the data acquisition, with all the telescopes and the optic fibers, was assembled and has undergone the calibration process.

5.3.1 RoIs definition

The first step of the calibration involves the definition of the $RoIs$ (regions of interest) of the spectrograph. Once the optic fibers have been accurately placed in the appropriate support, the slit is then closed to attain a $50\mu m$ opening. The size is small enough for the signal not to saturate (or a visible flat top would show), to have a Gaussian shape and to avoid background noise.
The image acquired by the camera, like the one in figure 17, that shows the light coming from the optical fibers, cut by the slit, is then divided into five regions of interest, one for each fiber. This allows to collect simultaneously data and spectra from each telescope individually with one camera.

The criteria applied for the definition of the RoIs are the following: some pixels above the first light rectangle, then the pixels between the first and the second rectangles were divided in half, one side belonging to the upper RoI and one half to the bottom one, making sure that no empty pixel rows were left outside one of RoIs. The same procedure was repeated till the last one, where some other pixels

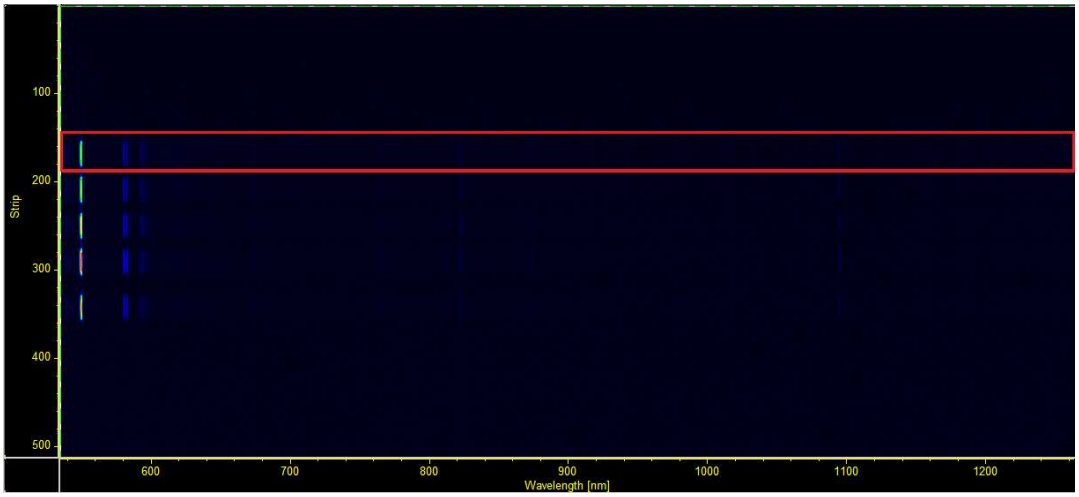

Figure 17: The definition of the first RoI for the grating with 50 *grooves/mm* around the 900 nm position, not calibrated. The light rectangles are the result of the light diffracted by the grating and collected by the camera.

below the lowest rectangle were taken.
After this procedure, for all the different gratings, the RoIs were checked in the full spectra, so that they do not contain light rectangles of different telescopes, or at least in the $(400 - 900)$ nm region, where the Balmer series and some second order wavelengths are present.

5.3.2 Zeroing

After the wavelength calibration, zeroing of the spectrograph is performed. By utilizing the ambient light, the spectrograph was placed at the zero position and the collection time was adjusted in order not to saturate the signal.
Since the order zero is due to the undispersed light that has not undergone diffraction by the gratings, it contains all the wavelengths present in the original light source.
Once the $zero - peak$ signal was detected, the gratings were manually rotated till the maximum corresponded with the pixel 1024, or half of the 2048 pixels of the camera.
The position of the gratings was then inserted in the hardware, so that no more zeroings are needed for the final procedures that were repeated multiple times.

5.3.3 Relation between grating motion and wavelength spanned

It is then necessary to define the relation between the motion of the gratings inside the spectrograph and the wavelength spanned. In order to do so, the telescopes were exposed to the light of a calibrated mercury lamp.
For the division, three wavelengths were chosen around the working zone, that could

be easily distinguishable. For the least diffractive grating, the second order of the 579.066nm, so the 1158.132 nm, was chosen, so that a valid result of the whole spectra could be achieved. For the other two gratings, the 579.066 nm line was chosen. Not only those wavelengths are really close to the zone of interest of the Balmer series and, since mercury emits a well distinguishable doublet at 576.959 nm and at 579.066 nm, they are really easy to find for both first and second order.

5.3.4 Calibration curve

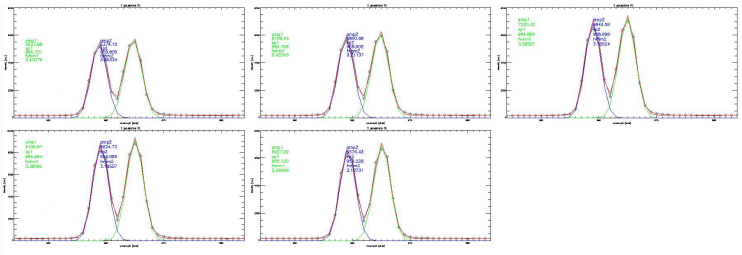

Figure 18: All the five signals from the RoIs of the doublet of the 576.959nm and 579.066nm emitted from the mercury lamp that was used for calibration purposes .

The last procedure for the wavelength calibration is to find the calibration curve. Since at different gratings positions, the correspondence between the number of pixels and the wavelength spacing is not the same, the last calibration parameters are to be found.

The spectrograph, for the calibration, utilizes the grating equation for the Czerny-Turner configuration, that can be written as follows:

$$\left(\frac{m}{d}\right)\lambda = sin\alpha + sin\beta \tag{5.5}$$

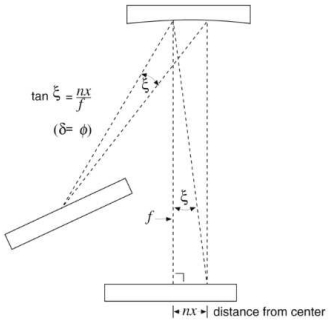

Figure 19: Czerny-Turner angles for wavelengths not in the centre of the image plane.

where λ is the wavelength at the center of the image plane m is the diffraction order, d is the distance between the grooves (the inverse of grooves per millimeter), α is the angle between the normal to the grating and the incident light and β is the angle between the normal to the grating and the diffracted light.

Those angles are related to the inclusion angle γ and the rotational angle of the grating, ψ by the following relations:

$$\alpha = \psi - \gamma/2 \tag{5.6}$$

Grating	Focal length (mm)	Inclusion angle (°)	Detector angle (°)
50 $grooves/mm$	750.6	13.45	0
100 $grooves/mm$	749.6	13.4	-0.05
900 $grooves/mm$	750.8	10.95	-0.05

Table 4: Table of parameters for calibration curve

$$\beta = \psi + \gamma/2 \tag{5.7}$$

$$\psi = asin(m\lambda/(2dcos(\gamma/2))) \tag{5.8}$$

Thus, the grating equation for the lambda at the center of the image plane can be written has:

$$\frac{m}{d}\lambda = sin(\psi - \gamma/2) + sin(\psi + \gamma/2) = 2sin(\psi)cos(\gamma/2) \tag{5.9}$$

For the wavelengths around the placed position of the spectrograph (or the wavelength at the center of the image plane), the previous equation needs to be adjusted:

$$\lambda^{'} = \left(\frac{d}{m}\right)(sin(\alpha) + sin(\beta + \xi)) = \left(\frac{d}{m}\right)(sin(\psi - \gamma/2) + sin(\psi + \gamma/2 + \xi)) \tag{5.10}$$

Where the ξ angle, as explained in figure 19 depends on the focal length f, the detector angle δ and the distance of the $\lambda^{'}$ wavelength from the center of the image plane, expressed as nx; here n is the number of pixel distance and x is the pixel width.

$$tg(\xi) = \left(\frac{nx}{f}\right) \tag{5.11}$$

if the image plane is perpendicular, otherwise:

$$tg(\xi) = \frac{(nx * cos(\delta))}{f + nx * sin(\delta)} \tag{5.12}$$

The parameters obtained from the calibration are reported in table 4.

5.3.5 Spectral Resolution

After the calibration is over, the last thing to define is the resolution of our spectrograph expressed as:

$$R = \frac{\lambda}{FWHM} \tag{5.13}$$

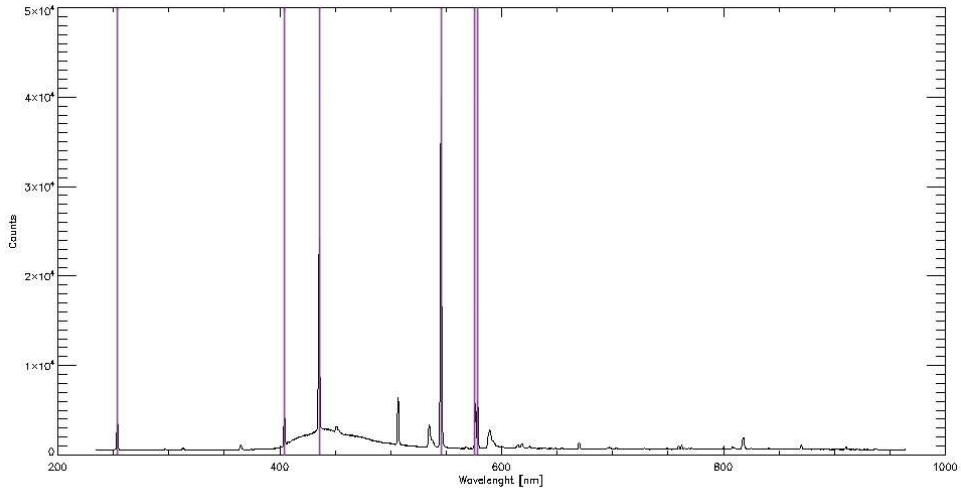

Figure 20: The calibrated spectrum recorded with the 50 *grooves/mm* grating with evidence of mercury emission lines of 253.652 nm, 404.656 nm, 435.833 nm, 546.075 nm, 576.961 nm and 579.067 nm.

Since different grating positions, inclinations of optical fibers and unwanted noise sources can give an amplitude, instead of a well defined peak, a Gaussian fit was executed over all the peaks of mercury emission and the $FWHM$ was calculated in order to find the smallest width possible. The peak with the smallest $FWHM$ should be a good indicator of the spectrograph resolution.

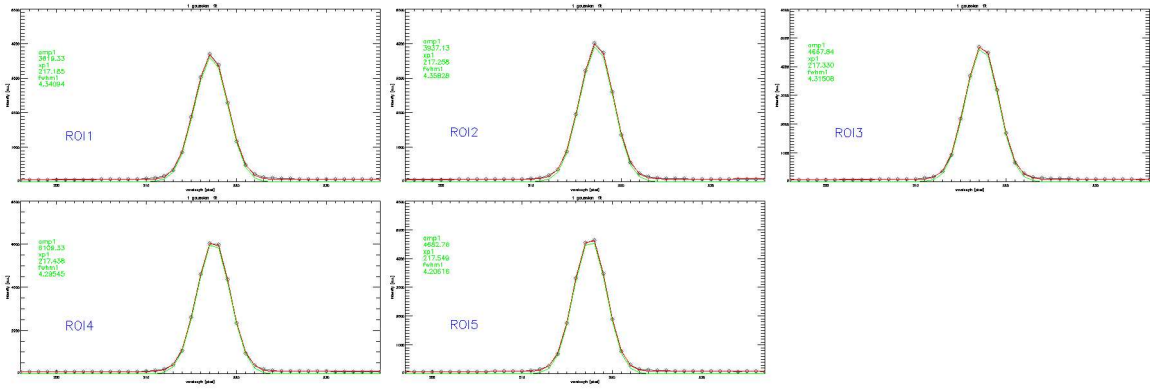

Figure 21: Gaussian fit for the 404.656 nm mercury emission line.

Between all the lines, the one with the thinnest peak was found to be the line 404.656 *nm*. The table reports the values of all the $FWHM$ for different RoIs for the line 404.656 *nm* for the three different gratings, the position in pixels of the peak and the corresponding calibrated wavelength.

RoI	FWHM (pixels)	$X_{peak}(pixels)$	$\lambda(nm)$
50 $grooves/mm$ 600nm			
1	3.13	477	404.67
2	3.14	477	404.7
3	3.13	477.1	404.74
4	3.14	477.3	404.78
5	3.12	477.4	404.82
100 $grooves/mm$ at 400nm			
1	3.45	1051.7	404.85
2	3.44	1051.8	404.87
3	3.4	1051.9	404.88
4	3.38	1052	404.90
5	3.34	1052.1	404.92
900 $grooves/mm$ at 420nm			
1	4.34	217.2	404.6
2	4.36	217.3	404.6
3	4.32	217.3	404.6
4	4.3	217.4	404.6
5	4.21	217.5	404.6

Table 5: Amplitude of the 404.656nm line for the three gratings.

5.4 Intensity calibration

For the first measures in plasma, it will be used a different setup. The spectrograph used is a Mini-Hamamatsu spectrometer, which has been calibrated in wavelength with the same procedure described before.

The intensity calibration was executed with a Helios LabSphere, which simulates the emission of a black body. With the telescope of 50 cm focal length that will be placed inside the MINION vessel, a background signal with the lamp off was recorded. Then, the lamp was turned on and the spectrum was recorded.

Knowing the number of photon emitted by the lamp, it is possible to convert the intensity data from arbitrary units into photons over seconds over square meters per wavelength.

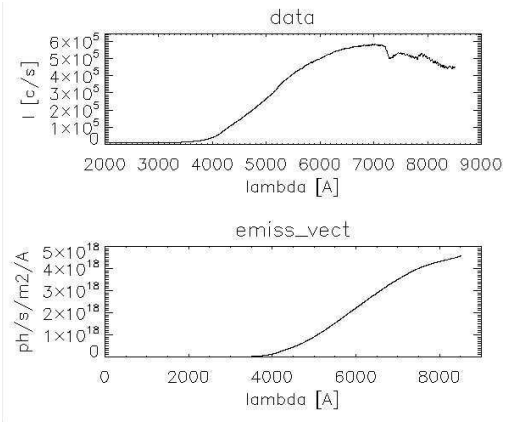

Figure 22: Lamp spectrum emission recorded in count per second.

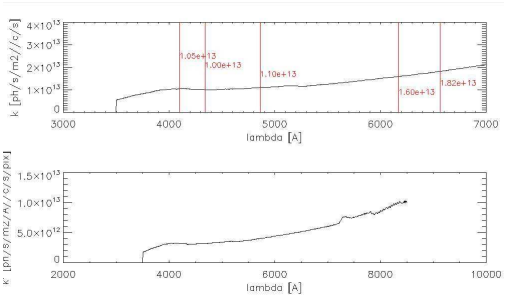

Figure 23: Calibration curves for data acquired by the spectrograph. In red are marked the coefficients for the conversion of the Balmer series.

6 Calibration of tungsten filament current

In the MINION experiment a tungsten filament is ignited in order to initiate the plasma. As voltage is applied across the filament, a current starts to flow and the filament heats up. The electrons possessing enough kinetic energy, given by the thermal agitation motion, can escape the metallic lattice (thermionic electrons). If the filament is negatively biased with respect to the surrounding surfaces, such electrons are accelerated away from the filament and can ionize the background gas, turning on the plasma.

The objective of the calibration of the tungsten filament is to understand the electron current it can emit and if it is sufficient to turn the plasma on.

Parameter	Symbol	Value
Length	L	178 mm
Diameter	d	0.25 mm
Tungsten resistivity	ρ	$5.60 * 10^{-8}$ Ωm
Resistance-temperature coefficient	β	0.94
Tungsten emissivity	ϵ_t	0.22

Table 6: Parameters for a tungsten filament

The thermal power heating the filament, as electric current goes through, is described by the Joule effect:

$$P_J = RI^2 \qquad\qquad P_J = VI \tag{6.1}$$

where R is the resistance of the filament, which is not constant over time, as it depends on the temperature. It is assumed that equation $R = \rho_0(1 + \alpha\Delta T)$ is not truly accurate for the filament; the following relation is adopted instead :

$$\frac{R_2}{R_1} = \frac{\rho_2}{\rho_1} = \left(\frac{T_2}{T_1}\right)^{\beta} \tag{6.2}$$

where ρ_1 is the tungsten resistivity at ambient temperature.
As the tungsten filament gets hotter and hotter, it starts to emit power following the Stefan-Boltzmann law:

$$P_r = \epsilon S \sigma_B T^4 \tag{6.3}$$

where ϵ is the relative emissivity of tungsten, in comparison to a black body that has emissivity $\epsilon = 1$, S is the exposed surface, σ_B is the Stefan-Boltzmann constant and T is the temperature of the filament.
Assuming that the electrons available for emissivity are the same available for con-

duction, the minimum amount of energy to bring an electron from Fermi level to $V = 0$ is called work function and depends on the material.
Once the temperature of the filament is known, it is possible to give an estimate of the emission current density with the Richardson and Dushman experimental law:

$$j_S = A_g T^2 e^{-W/k_B T} \tag{6.4}$$

where $A_g = \lambda_R A_0$ is the Richardson constant, in which λ_R depends on the cathode material, W is the work function, k_B is the Boltzmann constant.
A first estimate of the temperature is obtained by considering that the power generated by the Joule effect is totally transformed in emission power.
This overestimates the true value of the temperature because the heat and current flow along the filament is not considered.
A more realistic model, which takes into account both heat diffusion in the filament by Joule effect and heat emission according to the Stefan-Boltzmann law, is represented by the following differential equation:

$$-\frac{d}{dx}\left(\Sigma k_T \frac{dT}{dx}\right) = \frac{c^2 \rho_T}{\Sigma} - 2\pi r_{filament} \sigma_B \epsilon (T^4 - T_0^4) \tag{6.5}$$

By fixing the border conditions of the temperature at the two extremities of the tungsten filament, it is possible to give an estimate of the filament thermal profile, and so an estimate of the density current flow.
This model has a shortcoming: when changing the border conditions by some hundreds Kelvin, the maximum temperature of the filament seems to tend to a saturation value and there are no relevant changes. As the filament is thermally isolated, it is difficult to give an appropriate estimate of the temperature of the filament extremities.
One additional method for estimating the temperature of the filament is by measuring the emission spectrum of the filament once it is hot enough and it emits photons in the visible region.
Since a 50 *cm* focal length telescope has been placed behind the driver region, it can be used to measure the light emitted by the filament. The setup described in the Intensity calibration section was used.

Figure 24 shows the spectrum acquired by the spectrograph. In order to convert the intensity from counts per second into photons over square meters per second, the calibration curve obtained during the intensity calibration was applied, after removing a background with the same integration time, which was useful to correct

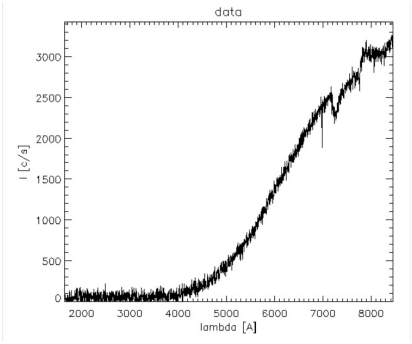

Figure 24: Raw spectrum acquired of the filament emission at 6 A.

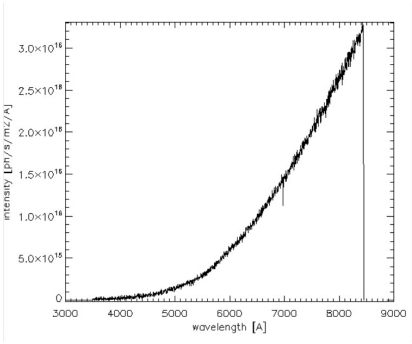

Figure 25: Calibrated data acquired of the filament emission at 6 A.

the data.

Then a fit of a Planckian function was done. In order to find the most probable temperature, plots of Planckian functions at different temperatures were done.

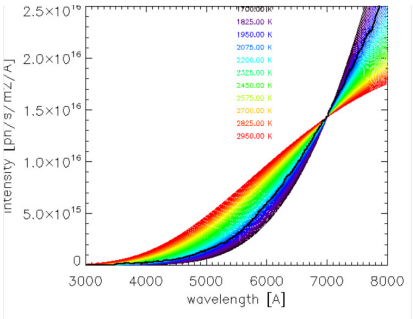

Figure 26: Plots for Planckian functions at different temperatures. The thickest black line is the fit from the data.

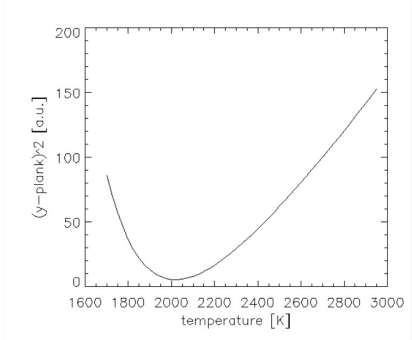

Figure 27: Quadratic residuals for different Planckian functions.

In figure 26 an example of data with a filament current of 6 A Planckian plots is shown. In figure 27 the squared residuals of the data with different curves is shown. The minimum of the curve gives the most probable temperature for the data acquired.

Figure 28 shows estimates of the temperature at different filament currents. As expected, if it is considered that the simple model that assumes that all heat is radiated overestimates the filament temperature with respect to spectroscopy, which can be used as a reference to compare the data with the heat diffusion model. In the figure several results are shown for different temperature of the filament supports. It can be seen that the supports can be around 500 C to justify the data, while the simulations with 800 C shows an overestimation of the temperature. However, since the model has some limits, like the fact that the filament extremities are in thermal

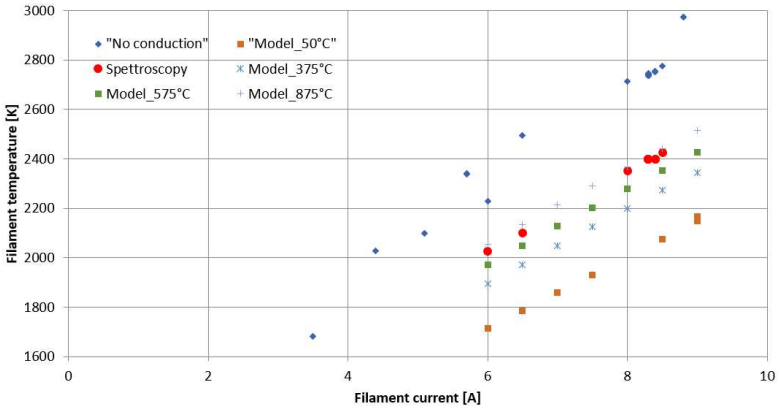

Figure 28: Confrontation between different emission models

contact with a cold region for some centimeters not only in a point with a fixed temperature, as well as the existence of a region, outside the thermal and electrical contact, where current is not conducted and the temperature is lower than the estimations. The aforementioned temperature of the filament extremities is compatible with the holder made of alumina that can withstand very high temperatures.

7 Characterization of vacuum and gas injection systems

The MINION vacuum system consists of (figure 29):

- one Screw pump ScrollVac 18 plus
- two cryogenic pumps 1500 CL, 2.5 m3/s in H_2 each, capacity 12 barL
- two turbomolecular pumps MAG-INTEGRA CF200 1300 iP

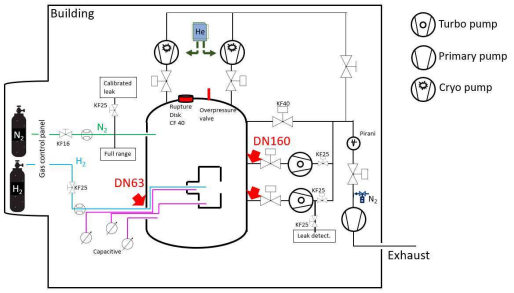

Figure 29: MINION vacuum system.

In figure 30 the expected pressures of the vessel and of the source for different gas flows are shown, knowing experimentally that with a gas flow of 50 *sccm* the total pumping speed is larger than 5 m^3/s. These values were experimentally verified.

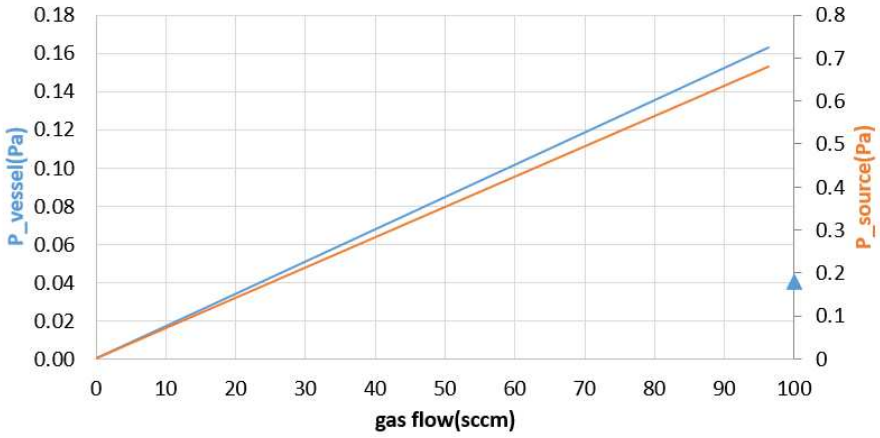

Figure 30: Gas flow vs Pressure

8 Conclusions

To attain nuclear fusion conditions, magnetically confined plasmas require other heating systems in addition to ohmic heating. One of them is represented by the injection of accelerated neutral beams. At the large beam particle energy for the ITER experiment (1 MeV), for efficient neutralization of the beam negative hydrogen ions must be used, which are created in a plasma source, powered by 8 radiofrequency drivers. Recent experimentation at the ITER Neutral Beam Test Facility in Padova showed that the present design of the source works properly, although it is hardly expected the required beam current density (330 A/m^2). Some optimizations are planned, including the enhancement of the plasma confinement, by installing permanent magnets around the RF drivers. To identify the most promising magnetic configuration, a test stand (dubbed $MINION$) was realised and the preparation of the experimental phase is on-going.

This thesis work was devoted to the preparation of the experiments in the MINION test stand. A capacitive probe was realised and calibrated. This way it was shown that it will be possible to measure the amplitude of the RF oscillations, which is usually compensated for by LC filters. Calibrating the plasma spectroscopy system will permit to interpret the light collected in different locations in the plasma.

During the thesis, activities preliminary to MINION operations were carried out:
- the calibration of the pre-ionization filament
- the verification of the pumping speed of the vacuum system.
I also contributed in collecting the data during the first day dedicated to plasma initiation; this test was carried out with the following settings:
- 30 mA filament current
- 0.6 Pa source pressure
- 25 kW RF power. Before starting the plasma initiation test, the RF circuit was tuned so as to avoid discharges around the RF coil.

In the next months, the activities preliminary to plasma initiation will be completed. After finding a proper recipe for plasma initiation:
- the experimentation with present magnetic configuration will start devoted to
- the assessment of plasma parameters as functions of the RF power
- the verification that no damages occur to Faraday shield during exposure to plasma
Finally other arrangements of the additional magnets will be prepared and compared, including the configuration without additional magnets.

9 Appendix

This Appendix contains the tables corresponding to some graphs shown in the thesis.

$f(MHz)$	$V_{gen}(V)$	$V_{probe}(V)$	$Attenuation$
26	3.00 ± 0.06	0.0145 ± 0.0006	0.0048 ± 0.0006
25	2.94 ± 0.06	0.0139 ± 0.0006	0.0047 ± 0.0006
24	3.26 ± 0.06	0.0147 ± 0.0006	0.0045 ± 0.0006
23	3.30 ± 0.06	0.0155 ± 0.0006	0.0047 ± 0.0006
22	3.96 ± 0.06	0.0174 ± 0.0006	0.0044 ± 0.0006
21	3.30 ± 0.06	0.0136 ± 0.0006	0.0041 ± 0.0006
20	3.57 ± 0.06	0.0150 ± 0.0006	0.0042 ± 0.0006
19	3.35 ± 0.06	0.0135 ± 0.0006	0.0040 ± 0.0006
18	3.70 ± 0.06	0.0140 ± 0.0006	0.0038 ± 0.0006
16	3.40 ± 0.06	0.0110 ± 0.0002	0.0032 ± 0.0002
15	3.27 ± 0.06	0.0102 ± 0.0002	0.0031 ± 0.0002
14	2.69 ± 0.06	0.0080 ± 0.0002	0.0030 ± 0.0002
13	2.20 ± 0.06	0.0064 ± 0.0002	0.0029 ± 0.0002
12	1.12 ± 0.02	0.0035 ± 0.0002	0.0031 ± 0.0002
10	0.70 ± 0.02	0.0025 ± 0.0002	0.0036 ± 0.0002
8	0.72 ± 0.02	0.0013 ± 0.0002	0.0017 ± 0.0002

Table 7: Data from probe calibration.

f (MHz)	Attenuation	$V_{pp}mV$	$V_{plasma}V$	SWR
28.0	0.0051 ± 0.0003	153	30 ± 2	4
28.2	0.0051 ± 0.0003	175	34 ± 2	3.3
28.4	0.0051 ± 0.0003	214	42 ± 2	2.9
28.6	0.0052 ± 0.0003	243	47 ± 3	2.6
28.8	0.0052 ± 0.0003	255	50 ± 3	2.25
29.0	0.0052 ± 0.0003	260	50 ± 3	1.9
29.2	0.0052 ± 0.0003	240	46 ± 3	2.1
29.4	0.0053 ± 0.0003	262	50 ± 3	1.7
29.6	0.0053 ± 0.0003	278	53 ± 3	1.3
29.8	0.0053 ± 0.0003	280	53 ± 3	1.25
29.99	0.0053 ± 0.0003	260	49 ± 3	3.2

Table 8: Data at fixed pressure and different frequencies

Distance (mm)	Measured diameter (mm)	Distance (mm)	Simulated diameter 90%	Simulated diameter 99%
550	4.25 ± 0.08	10	9.34	9.82
525	4.25 ± 0.08	41.0526	8.78	9.31
500	4.25 ± 0.08	72.1053	8.25	8.86
475	4.50 ± 0.08	103.158	7.74	8.46
450	4.50 ± 0.08	134.211	7.27	8.07
425	5.00 ± 0.08	165.263	6.82	7.68
400	5.00 ± 0.08	196.316	6.40	7.32
375	5.50 ± 0.08	227.368	6.00	6.95
350	5.50 ± 0.08	258.421	5.63	6.60
325	5.50 ± 0.08	289.474	5.27	6.26
300	6.00 ± 0.08	320.526	4.94	5.92
275	6.00 ± 0.08	351.579	4.64	5.59
250	6.00 ± 0.08	382.632	4.36	5.28
225	6.50 ± 0.08	413.684	4.11	4.97
200	6.75 ± 0.08	444.737	3.90	4.68
175	7.00 ± 0.08	475.789	3.74	4.41
150	7.50 ± 0.08	506.842	3.66	4.17
125	7.50 ± 0.08	537.895	3.63	3.98
100	7.50 ± 0.08	568.947	3.95	4.27

Table 9: Data of measured diameters and simulated diameters for the $50cm$ focal and $10mm$ diameter lens.

10 Bibliography

U. Fantz, *Basics of plasma spectroscopy*, Plasma Sources Sci. Technol. **15** (2006) S137–S147

L. Ferbel, *First plasma operations of the SPIDER experiment*, Bachelor thesis, University of Padova, academic year 2017-2018

I. Mario *et al.*, *Optimizing the ITER NBI ion source by dedicated RF driver test stand*, 2023, submitted to Journal of Physics; Conference Series

C. Poggi *et al.*, *CRISP: A compact RF ion source prototype for emittance scanner testing*, Rev. Sci. Instrum. **91** (2020) 033314

S. E. Savas, K. G. Donohoe, *Capacitive probes for rf process plasmas*, Rev. Sci.lnstrum. **80** (1989) 3391

I. D. Sudit and F. F. Chen, *RF compensated probes for high − density discharges*, Plasma Sources Sci. Technol. **3** (1994) 162

D. Wünderlich, S. Dietrich, U. Fantz, *Application of a collisional radiative model to atomic hydrogen for diagnostic purposes*, Journal of Quantitative Spectroscopy & Radiative Transfer **110** (2009) 62–71

B. Zaniol, R. Pasqualotto, and M. Barbisan, *Design of a beam emission spectroscopy diagnostic for negative ions radio frequency source SPIDER*, Rev. Sci. Instrum. **83** (2012) 043117